Bioinorganic Chemistry and Applications

WILEY

RESEARCH ARTICLE OPEN ACCESS

Shape-Directed Hydrothermal Design of Zinc Oxide Nanoparticles for Antimicrobial and Anticancer Applications

Elvan Hasanoğlu Özkan[1] | Nurdan Kurnaz Yetim[2] | Hamit E. Kızıl[3] | Hatice Öğütçü[4,5]

[1]Department of Chemistry, Faculty of Science, Gazi University, Teknikokullar 06500, Ankara, Türkiye | [2]Department of Chemistry, Faculty of Arts and Sciences, Kırklareli University, Kırklareli, Türkiye | [3]Department of Medical Services and Techniques, Vocational School of Health Services, Bayburt University, Bayburt, Türkiye | [4]Department of Field Corps, Faculty of Agriculture, University of Kırşehir Ahi Evran, Kırşehir, Türkiye | [5]Department of Biology, Polatlı Faculty of Science and Letters, AnkaraHacı Bayram Veli University, Ankara, Türkiye

Correspondence: Elvan Hasanoğlu Özkan (ehasanoglu@gazi.edu.tr)

Received: 6 October 2025 | **Revised:** 28 December 2025 | **Accepted:** 27 January 2026

Academic Editor: Massimiliano F. Peana

Keywords: antimicrobial activity | antimicrobial resistance | hydrothermal method | pathogenic microorganism | ZnO-NPs

ABSTRACT

The emergence of antibiotic-resistant bacteria represents one of the most pressing challenges in global healthcare. In this study, metal oxide–based nanomaterials are gaining prominence due to their antimicrobial and anticancer potential. In the present study, six new zinc oxide nanoparticles (ZnO-NPs) synthesized via the hydrothermal method using different surfactants were characterized, and their biological activities were evaluated. ZnO-NPs, whose structural properties were determined by a range of analytical methods including BET, FT-IR, SEM-EDX, XRD, and XPS, exhibited significant antibacterial and antifungal effects on a range of bacterial and fungal strains. The study revealed that variations in the morphology and surface area had a direct impact on antimicrobial efficacy. In antimicrobial assays, the inhibition zones ranged from 10.5 mm to 25.5 mm, with ZnO-6 exhibiting the highest efficacy against *S. epidermidis* (25.5 mm). In cytotoxicity assays, ZnO-6 demonstrated the strongest anticancer potential against H460 cells with the lowest IC_{50} value of 31.9 μg/mL. Furthermore, a strong correlation was revealed between the physicochemical properties of ZnO-NPs and their anticancer activity, as evidenced by the results of tests conducted on H460 lung cancer cells. Specifically, ZnO-6, which possesses a flower-like morphology and the highest surface area, exhibited the strongest anticancer effect with an IC_{50} value of 31.9 μg/mL. The parallel enhancement in both antimicrobial and anticancer activities observed in ZnO-6 suggests a common underlying mechanism, likely driven by the high surface area and specific flower-like morphology that facilitates increased interaction with cell membranes and ROS generation. The findings demonstrate that the controlled design of ZnO-NPs in terms of morphology and surface area offers significant potential in both antimicrobial and anticancer applications.

1 | Introduction

The unconscious and unnecessary use of antimicrobial drugs, combined with inadequate implementation of infection control measures, has accelerated the spread of multidrug-resistant microorganisms, making antimicrobial resistance a global health problem. In the face of this problem, an urgent need has arisen to develop more effective and innovative antibiotics [1]. Statistics shared by the World Health Organization (WHO) show that lower respiratory tract infections and digestive system infections are among the leading causes of disease and death

worldwide [2]. The emergence of microorganisms that have become resistant to antibiotics significantly complicates both the lethality and clinical management of these infections. It is noteworthy that today, the number of deaths due to resistant bacteria exceeds the total number of deaths from cancer and diabetes [3]. Despite the wide range of antibiotic options, resistance to almost all of them has developed, reducing the effectiveness of the current treatment approaches. In addition, the emergence of resistance to even newly developed antibiotics in a short time shows that this problem requires sustainable solutions [4]. In line with all these developments, the WHO put into effect the Global Action Plan against Antimicrobial Resistance in 2015 [5].

Secondary bacterial infections observed in intensive care units can lead to increased mortality among patients in intensive care, particularly in those with bacterial coinfection and secondary infections, such as COVID-19 [6, 7]. Lung cancer remains the leading cause of cancer-related deaths worldwide, necessitating the development of novel therapeutic agents with reduced systemic toxicity. Similarly, fungal infections, particularly those caused by *Candida* species, represent a growing threat in immunocompromised patients, often complicating viral or bacterial pneumonia. This makes the development of new antimicrobial compounds a priority issue for global public health.

Advances in biomedical materials, including biomarkers, biosensors, and drug delivery systems, can be improved by changing their shape, size, and surface properties [8]. At this point, nanoparticles (NPs) stand out, thanks to their small size. Their high surface-to-volume ratio, their similarity to biomolecules, and their ability to pass through cell membranes make them ideal biomaterials [9–11]. Particle morphology and specific surface area are very important for antibacterial activity, as these properties increase the interacting surface size and binding sites. Therefore, developing new materials with high surface area and optimized morphology has great potential for biomedical applications [12, 13].

Various methods have been reported in the literature for producing NPs for specific applications. Each production method has certain pros and cons. For example, UHV-based methods, such as magnetron sputtering, gas aggregation, and sputter-based methods, can produce quite pure NPs with minimal contamination [14–16]. Such methods can also provide high control over particle size and particle formation, allowing for the production of NPs with precise compositions. However, such methods are not suitable for mass production since the capacity of such systems is limited. Moreover, such systems are quite expensive and require high expertise. On the other hand, chemical-based methods, such as chemical reduction, hydrothermal synthesis, and solgel synthesis, are common methods used for NP production [17, 18]. These methods enable researchers to produce a large number of NPs in a limited time with good quality. Furthermore, such methods are facile, economical, and fast and do not require high expertise. However, chemical-based methods do not provide atom-by-atom precision, and the NP morphology can be affected by production conditions. Therefore, verification of these properties is important to expand the field of use of the material. Additionally, reducing particle size is an effective way to increase surface area. Among nanomaterials, metal oxides are frequently preferred due to their biocompatibility and stability [19, 20]. Many metal oxide NPs, such as silver (Ag), gold oxide (AuO), titanium dioxide (TiO_2), zinc oxide (ZnO), copper oxide (CuO), and cerium oxide (CeO_2), are used in biomedical applications. For example, gold NPs are utilized in medical applications, including diagnostics and photothermal therapy [21]. Gold NPs can enhance the contrast in x-ray and computed tomography imaging, making them a preferred contrast enhancement agent. Similar characteristics are also evidenced by Bi-based NPs, as they exhibit high x-ray attenuation properties [22]. Bi-based materials have been reported as photoactive materials and can therefore be used as photothermal agents in cancer therapy applications. Fe-based materials were used in MRI applications since Fe-based NPs can enhance the contrast of the injected tissues. Furthermore, Fe-based NPs with superparamagnetic characteristics can exhibit magnetic hyperthermia characteristics [23]. Regarding these characteristics, Fe-based NPs can be utilized as theranostic agents, enabling the simultaneous delivery of diagnostic and therapeutic effects. Among these, ZnO-NPs stand out due to their wide range of applications and remarkable properties [24]. Nanostructured ZnO has both optical and electrical properties [25] and has been shown to have cytotoxic effects against some cancer cells. Additionally, ZnO-NPs are preferred as one of the most common drug delivery systems due to their biocompatible structures. The U.S. Food and Drug Administration (FDA) has defined bulk ZnO as a substance generally recognized as safe, and ZnO-NPs with a particle size greater than 100 nm have been deemed relatively biocompatible and approved as drug delivery systems [26, 27]. ZnO-NPs can be synthesized using various chemical routes, including the hydrothermal method, solgel technique, coprecipitation, combustion, and sonochemical synthesis [28–30]. Among these methods, hydrothermal synthesis is important because it allows to obtain particles with high crystal quality at temperatures below 200°C [31, 32]. In addition, this method can be used to directly and purely synthesize in the solution, and high-quality thin films can be obtained. These features are the elements that make the hydrothermal method stand out in the production of nanomaterials [33]. Numerous ZnO structures with different morphologies have been described in the literature [34, 35]. These structures have shown varying catalytic performances depending on factors such as surface area, surfactant properties, and reducibility [36–40]. Therefore, investigating the effects of changes in the morphology on the antibacterial activity and biocompatibility of ZnO may further increase the potential of this material in the biomedical field. The H460 human lung cancer cell line was selected for this study, as inhalation represents a primary route of exposure to airborne NPs, making the assessment of biocompatibility and toxicity on lung tissue critical. Regarding the antimicrobial mechanism, ZnO-NPs are known to generate reactive oxygen species (ROS) such as hydrogen peroxide and hydroxyl radicals and release Zn^{2+} ions, which disrupt bacterial cell membranes and inhibit enzymatic functions [2, 3].

The aim of this study is to reveal the relationship between the morphological and physicochemical properties of six different morphologies of ZnO-NPs synthesized using different surfactants via the hydrothermal method [41–44] and their antimicrobial and anticancer activities. In this context, the antibacterial and antifungal effects of ZnO-NPs against Gram-positive and Gram-negative bacteria and yeast species were investigated. Additionally, their cytotoxicity was evaluated in the H460 human lung

cancer cell line. The innovative aspect of the study lies in the comparative evaluation of the antimicrobial and anticancer activities of ZnO-NPs with different morphologies within the same systematic approach, as well as the direct correlation of these biological activities with the NP morphology and surface area. The results show that the ZnO-6 sample, which has a high surface area and a flower-like morphology, exhibits the highest biological activity. That surface area plays a decisive role in both biological effects.

2 | Materials and Methods

2.1 | Synthesis of the ZnO-NPs

For the synthesis of ZnO-1, 1.09 g zinc acetate dihydrate was dissolved in 25 mL of ultrapure water. To the resulting solution, 0.5 mL ethylenediamine was added, and the pH of the solution was adjusted to 12 using 2.0 M NaOH. The mixture was stirred homogeneously using a magnetic stirrer for 30 min. The prepared solution was then transferred to a Teflon-coated autoclave reactor, and hydrothermal treatment was performed at 150°C for 12 h (Figure 1). After the treatment, the sample taken from the autoclave was transferred to a centrifuge tube and centrifuged at 8000 rpm for 5 min. The powder product obtained was purified by washing twice with ultrapure water and twice with ethanol. After washing, the sample was dried in an oven at 80°C for 12 h. The dried sample was placed in a muffle furnace at 320°C for 2 h for calcination. As a result of these processes, ZnO-1 was obtained. The same procedure was repeated using different solvents (ethanol; ZnO-2, butanol; ZnO-3, and propanol; ZnO-4) [41].

For ZnO-5 synthesis, 2.19 g of zinc acetate dihydrate ($Zn(CH_3COOH).2H_2O$) salt was accurately weighed using an analytical balance. In another beaker, 1.0 g of polyethylene glycol (PEG) was dissolved in 20 mL of ultrapure water to form a clear solution. Upon preparing the PEG solution, zinc acetate dihydrate was slowly dissolved therein. 0.5 M urea solution (20 mL) was subsequently poured in dropwise to prepare the mixtures. After the reaction was complete, the solution was transferred to a Teflon-coated autoclave reactor and heated to 150°C in an oven for 12 h. After heating, the sample was transferred to a centrifuge tube and centrifuged at 8000 rpm for 5 min. The solid product obtained was purified by washing twice with ultrapure water and twice with ethanol. The sample was then dried in an oven at 80°C for 12 h. Finally, the dried sample was calcined in a muffle furnace at 320°C for 2 h. As a result of these processes, the ZnO-5 sample was obtained [42, 43].

In another synthesis, 7 mL of glycerol, 7 mL of ethyl alcohol, and 10 mL of ultrapure water were mixed to form a homogeneous solvent medium. Weighed 0.52 g zinc nitrate hexahydrate ($Zn(NO_3)_2\ 6H_2O$) and 0.8 g sodium hydroxide (NaOH) were added to this mixture. The prepared solution was stirred on a magnetic stirrer for 1 h, then transferred to a Teflon-coated autoclave reactor, and subjected to hydrothermal treatment in an oven at 120°C for 12 h. At the end of the process, the sample taken from the autoclave was transferred to a centrifuge tube and centrifuged at 9000 rpm for 10 min. The powdery product was purified by washing twice with ultrapure water and twice with ethanol. The washed sample was dried in an oven at 80°C for 12 h and then calcined in a muffle furnace at 450°C for 2 h to obtain ZnO-6 [41, 42].

2.2 | Spectral Data Measurements

A Rigaku MiniFlex 600 x-ray diffractometer equipped with a Ni-filtered Cu Kα source was utilized to determine the x-ray diffraction (XRD) patterns over a scan range of $10° < 2\theta < 90°$. The obtained peaks were compared with those reported in the literature and measurement cards. Using such data, elemental and crystal structure analyses were obtained. The infrared spectrum was recorded on a Jasco FT-IR 6700 spectrometer, over the

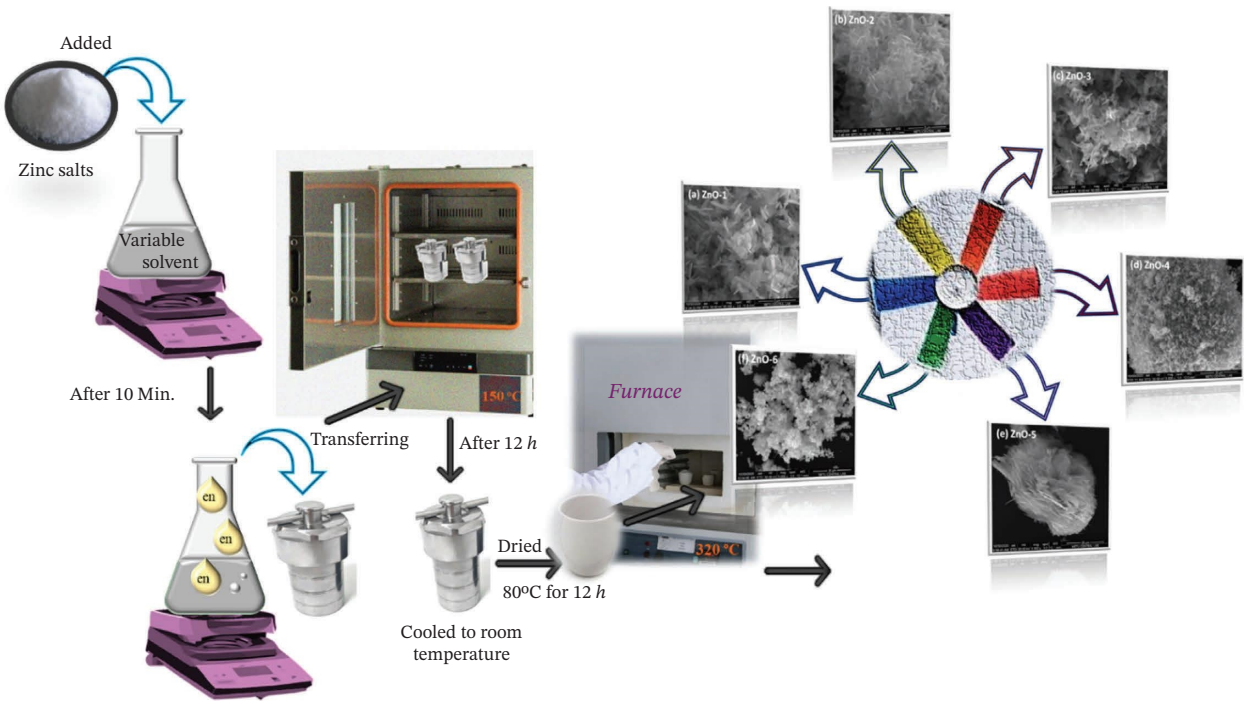

FIGURE 1 | Synthesis route of the ZnO-NPs.

wavelength range of 4000 to 400 cm^{-1}. Bands and peaks obtained from spectra were compared with similar results previously reported in the literature. Additionally, scanning electron microscopy (SEM) was employed to examine the surface morphology of the ZnO structures. The SEM images were obtained at 5000X and 50000X magnification using electrons with a 30 kV potential. Images were obtained using an aperture spot size of 3. No premeasurement process was employed on the samples before the SEM measurement. Energy-dispersive x-ray spectroscopy (EDX) was employed for determining the elemental composition of the ZnO structures. EDX scan was used for the 0–12 keV range. An FEI Quanta 400F model device was utilized for the SEM–EDX analyses. To examine the surface area of the nanostructures, the Brunauer–Emmett–Teller (BET) analysis was adopted. For this purpose, a Quantachrome Corporation Autosorb-6 device was utilized. BET investigations were performed between 0 and 1 P/P_0 relative pressure, where the adsorption and desorption characteristics of NPs were obtained.

2.3 | Analysis of the Antimicrobial Potential of ZnO-NPs

2.3.1 | Test Microorganisms

The pathogenic bacterial cultures *B. cereus* RSKK863, *E. coli* ATCC1280, *E. aerogenes* sp., *S. aureus* ATCC25923, *S. typhi* H NCTC901.8394, *S. epidermidis* ATCC12228, *M. luteus* ATCC9341, *L. monocytogenes, K. pneumoniae* ATCC 27853*, P. vulgaris* RSKK 96026, *P. aeroginosa* ATCC27853, and yeast (*C. albicans* Y-1200-NIH) were used. In all assays, standard antibiotics (sulfamethoxazole, kanamycin, ampicillin, amoxicillin, and nystatin) served as positive controls, while pure DMSO was used as a negative control to ensure the validity of inhibition zones.

2.3.2 | Detection of Antimicrobial Activity

The well diffusion method was utilized to examine the antimicrobial activity of ZnO-NPs against six Gram-negative bacteria (*S. typhi*, *E. coli*, *E. aerogenes* sp., *K. pneumoniae*, *P. vulgaris*, and *P. aeroginosa)*, five Gram-positive bacteria (*B. cereus, M. luteus*, *L. monocytogenes, S. aureus,* and *S. epidermidis*), and one yeast (*C. albicans*). The NPs were kept dry at room temperature and dissolved (100 μg/mL and 200 μg/mL) in DMSO. DMSO was utilized as the solvent for the compound and the control. It was determined that DMSO had no antimicrobial activity against any of the pathogenic microorganisms. A 1% (v/v) 24 h broth culture (containing pathogenic bacteria and yeast) at a concentration of 10^6 cfu/mL was placed on a sterile plate. Mueller–Hinton agar (15 mL) at 45°C was poured into Petri dishes and allowed to cool and solidify. Then, 6-mm-diameter wells were carefully drilled utilizing a sterile cork drill and filled with the synthesized ZnO-NPs and incubated for 24 h at 37°C to simulate physiological conditions for biomedical relevance [45–47]. At the end of incubation, the average of the two wells was utilized to calculate the growth inhibition zone of each pathogenic bacteria and yeast (to compare the degree of inhibition, bacteria and yeast were tested for resistance to antibiotics (sulfamethoxazole, kanamycin, ampicillin, and amoxicillin) and one anticandidal (nystatin) [48–50].

2.4 | Cytotoxicity assessment

Human lung cancer H460 cells were sourced from ATCC (USA) and cultured in T25 flasks (Jet Biofil, Guangzhou, China). The growth medium consisted of L-glutamine-containing RPMI 1640 (Gibco Thermo Fisher Scientific, USA) with 10% FBS supplementation (Gibco; Thermo Fisher Scientific, USA). Cell detachment for passaging involved washing with PBS (Merck | KGaA, Darmstadt, Germany) followed by trypsinization using trypsin-EDTA (Gibco | Thermo Fisher Scientific, USA). Incubation occurred at 37°C with 5% CO_2 for 48 h between passages. Viability monitoring utilized trypan blue staining (Merck | KGaA Darmstadt, Germany) with hemocytometer counting after centrifugation and resuspension. Metabolic activity was assessed using a tetrazolium-based method, in which living cells reduce these compounds via mitochondrial enzymes to produce colored formazan. Dead cells cannot perform this reduction, resulting in color intensity that is proportional to cell viability. The WST-8 protocol was performed using CVDK-8 reagent (Ecotech Biotechnology Erzurum, Türkiye) per the manufacturer's guidelines. Absorbance measurements of the orange formazan were taken with a Multiskan GO spectrophotometer (Thermo Fisher Scientific, USA) [51, 52].

2.5 | Statistical Analysis

All experiments were performed in triplicate, and the values are expressed as mean ± SD. The average and standard deviation of the diameter of the inhibition zone were determined by GraphPad Prism version 8.0.1 (GraphPad, San Diego, CA). One-way ANOVA was used for group comparisons in antimicrobial assays, while Student's *t*-test was employed for cytotoxicity analysis. A p value < 0.05 was considered statistically significant.

3 | Results and Discussion

3.1 | Sample Characterization

Figure 2 shows the XRD patterns of the synthesized ZnO-NPs. The intensity data were collected in the 2θ range of 10°–90°. In the figure, diffraction peaks at 31.8°, 34.5°, 36.3°, 47.8°, 56.7°, 63.0°, 66.7°, 68.1°, and 69.2° were identified which indicate and (100), (002), (101), (102), (110), (103), (200), (112), and (201)

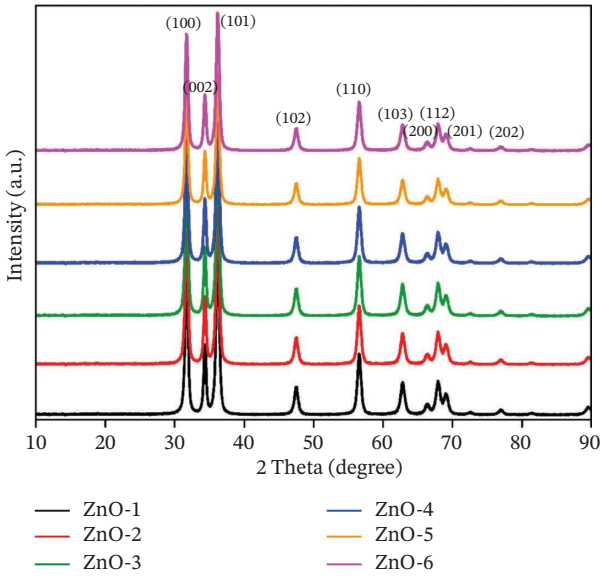

FIGURE 2 | XRD pattern of ZnO nanoparticles.

formation, respectively. The peak positions can be associated to wurtzite ZnO [41, 42, 44].

The high purity of the samples synthesized by hydrothermal is indicated by the sharp peak points in the XRD pattern and the absence of broad peaks in Figure 2.

The presence of Zn-O tension bands in ZnO structures was confirmed by the FT-IR spectrum, which showed the absorption peaks. Figure 3 shows the FT-IR spectra at room temperature of ZnO structure samples. FT-IR analysis is used as a verification method to ensure that the prepared materials contain the expected functional groups.

The ZnO structures mainly form a tape of approximately 580 cm^{-1} due to the stress vibrations of the Zn-O band, which confirms the formation of ZnO spinel oxide. The large band, which is centered at 3400 cm^{-1}, belongs to the O-H stretch vibration of adsorbed H_2O molecules and surface hydroxyl groups [41, 42].

The surface morphology of ZnO-NPs was examined using a field emission scanning electron microscope (FESEM) with an area of emission scanning at a scale of 2 μm to 20 μm, as shown in Figure 4. Figures 4(a), 4(b), and 4(c) show the irregular form of ZnO-NPs of 120–250 nm with an average size of 140 nm. NPs are found to be in a flake-like form, which are in ellipsoid shapes. These nanoflakes come together and produce agglomerated flake piles. Figure 4(d) shows ZnO-4-NPs. These NPs were in the form of a clover leaf. The figure illustrates that such flower-like structures agglomerate and form big NP piles. The size of individual alfalfa-like formations was between 400 and 1000 nm. In Figure 4(e), nanoplates with a diameter of 5–10 microns of the ZnO-5 appear to come together to form flower-like structures. Despite the large surface size of the plates, the thickness was found to be quite low (lower than 100 nm). Large gaps between plate-like structures can be identified by visual inspection. This physical feature allows the expansion of the active surface area of nanostructures with enhanced porosity. When the SEM image of the ZnO-6 in Figure 4(f) is examined, flower-like structures are identified. Such structures consist of NPs and nanospikes.

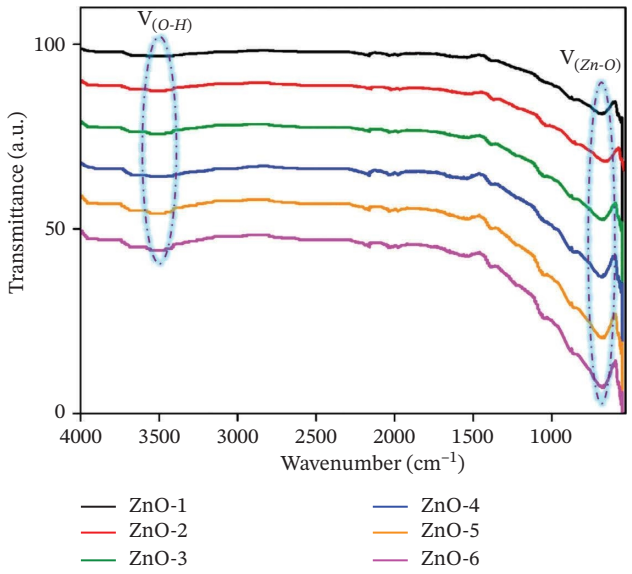

FIGURE 3 | FT-IR spectrum of ZnO nanoparticles.

Agglomeration of such structures forms gypsophila-like formations. NPs and nanospikes are less than one micron and 2–10 microns.

The element composition of the synthesized sample was determined using the EDX, as shown in Figure 5. The EDX spectrum reveals the presence of zinc and oxygen elements with a small amount of carbon. The presence of carbon is caused by the carbon band used to prepare FESEM and EDX samples.

The surface characteristics of ZnO-NPs were investigated by the N_2 gas adsorption–desorption method at 77 K, while the surface areas were investigated by the BET method, and the pore volume distribution was calculated according to the Barrett–Joyner–Halenda (BJH) method, and isotherms are presented in Figure 6. The specific surface area of the samples was calculated by the BET method, and for ZnO-1, ZnO-2, ZnO-3, ZnO-4, ZnO-5, and ZnO-6, respectively, 133.769 m^2/g, 590.779 m^2/g, 567.809 m^2/g, 34.2176 m^2/g, 298.41 m^2/g, and 1641.7 m^2/g. Compared to the literature data, ZnO-NPs structures have a wide surface area [53]. Previously, Ismail et al. reported an average surface area for ZnO-NPs as 8.8187 m^2/g, Abdolahi et al. produced Mg-doped ZnO-NPs and the particle surface area was determined as 4.3737 m^2/g, Shamhari et al. produced ZnO-NPs using the solvothermal method and determined the particle surface area as 101.32 m^2/g, and Brian et al. found the surface area of ZnO-NPs as 105.0 m^2/g [53–56]. It was seen that our NPs have much greater surface areas than that results reported in the literature.

3.2 | Antibacterial Activity

ZnO-NPs with different surface morphologies from each other showed variable growth activity (10 mm to 26 mm) for the pathogenic microorganisms used (Figure 7). Moreover, ZnO-NPs were more effective against Gram-negative bacteria than against Gram-positive bacteria.

The antimicrobial activities of six different ZnO-NP formulations (ZnO-1 through ZnO-6) were systematically evaluated against a panel of Gram-positive and Gram-negative bacteria, as well as a pathogenic yeast (*C. albicans*). The inhibition zones for each microorganism and ZnO-NP group were measured and are presented as mean ± standard deviation (SD). Overall, all ZnO-NP groups demonstrated measurable antimicrobial activity, with inhibition zones generally ranging from approximately 10.5 mm to 25.5 mm, depending on the microorganism and the specific ZnO-NP formulation. Among the Gram-positive bacteria, *S. epidermidis* was the most susceptible, with the highest inhibition zone observed for the ZnO-6 group (25.50 ± 0.71 mm), followed by ZnO-1 and ZnO-2 (both 21.50 ± 0.71 mm). *M. luteus* also showed relatively high sensitivity, with the largest inhibition zone for ZnO-5 (23.50 ± 0.71 mm), while the lowest values were observed for ZnO-5 and ZnO-6 (both 12.50 ± 0.71 mm). For *S. aureus*, inhibition zones ranged from 10.50 ± 0.71 mm (ZnO-5) to 19.50 ± 0.71 mm (ZnO-2 and ZnO-6). *B. cereus* exhibited moderate sensitivity, with inhibition zones between 11.50 ± 0.71 mm (ZnO-5) and 17.50 ± 0.71 mm (ZnO-3). *L. monocytogenes* showed inhibition zones from 15.00 ± 0.00 mm (ZnO-5) to 20.00 ± 0.00 mm (ZnO-6). For Gram-negative bacteria, the inhibition zones were generally lower and more variable. *P. aeruginosa* was only inhibited by ZnO-1, ZnO-2, and ZnO-3, with inhibition zones of 15.00 ± 0.00 mm, 16.50 ± 0.71 mm, and 16.00 ± 0.00 mm, respectively; no activity was observed for the

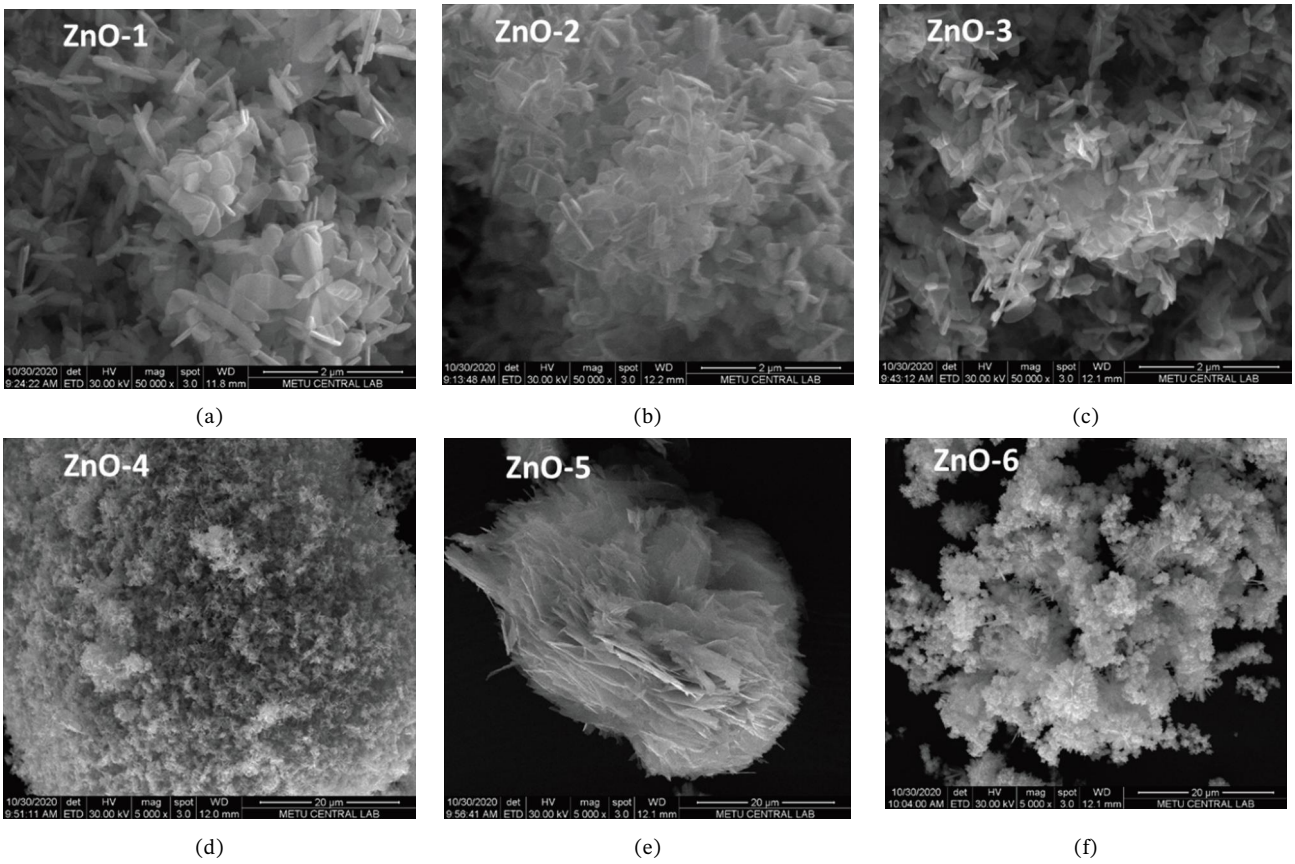

FIGURE 4 | The SEM images of (a) ZnO-1, (b) ZnO-2, (c) ZnO-3, (d) ZnO-4, (e) ZnO-5, and (f) ZnO-6.

other groups. *K. pneumoniae* showed the highest inhibition with ZnO-3 (23.50 ± 0.71 mm), while the lowest was with ZnO-5 (11.00 ± 0.00 mm). *E. aerogenes* was most susceptible to ZnO-5(21.00 ± 0.00 mm) and least to ZnO-9 (15.50 ± 0.71 mm). *S. typhi* inhibition zones ranged from 13.00 ± 0.00 mm (ZnO-5) to 18.50 ± 0.71 mm(ZnO-2). *E. coli* showed the highest inhibition with ZnO-1 and ZnO-3 (both 20.00 ± 0.00 mm) and the lowest with ZnO-6(11.50 ± 0.71 mm). *P. vulgaris* exhibited the lowest overall sensitivity, with inhibition zones ranging from 10.00 ± 0.00 mm(ZnO-3) to 12.00 ± 0.00 mm(ZnO-6). For the pathogenic

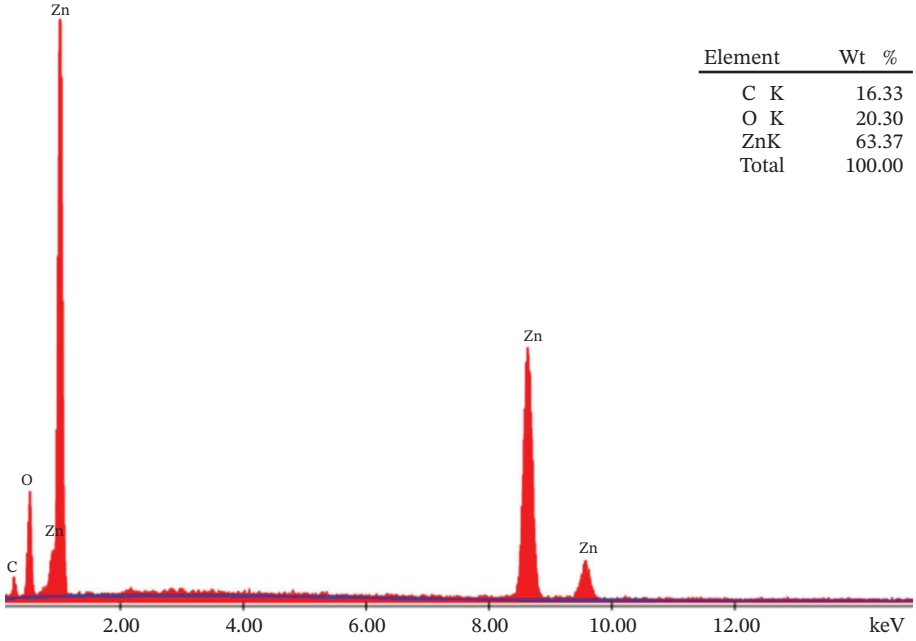

Element	Wt %
C K	16.33
O K	20.30
ZnK	63.37
Total	100.00

FIGURE 5 | EDX spectrum of ZnO-NPs.

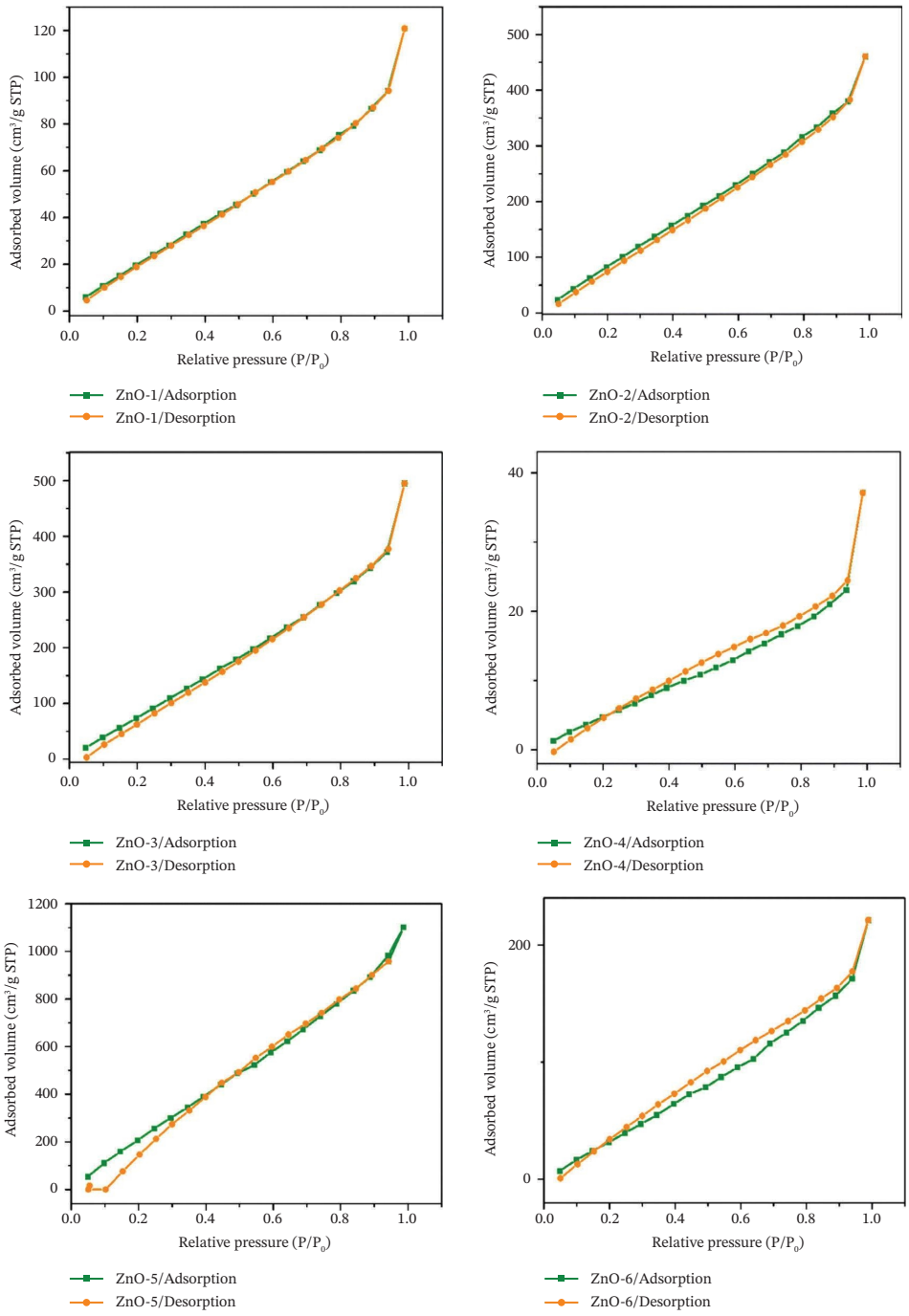

FIGURE 6 | Adsorption–desorption isotherms of ZnO-NPs.

yeast *C. albicans*, all ZnO-NP groups demonstrated significant antifungal activity, with inhibition zones ranging from 15.00 ± 0.00 mm (ZnO-5) to 21.50 ± 0.71 mm(ZnO-6). The highest activity was observed for ZnO-6, followed by ZnO-1 (21.00 ± 0.00 mm) and ZnO-4 (20.50 ± 0.71 mm). Statistical analysis using one-way ANOVA revealed that although differences in inhibition zone diameters were observed among the different ZnO-NP groups for some microorganisms, these differences were not statistically significant in most cases ($p > 0.05$). This suggests that while the antimicrobial efficacy of ZnO-NPs may vary slightly depending on the formulation and the target microorganism, no single ZnO-NP group demonstrated a consistently superior effect across all tested pathogens.

The comparative analysis of the six different ZnO-NP formulations highlights the significant impact of synthesis methods on the antimicrobial properties of metal oxide NPs. As observed in the results, ZnO-NPs synthesized with different solvents and stabilizers (H_2O, C_2H_5OH, C_4H_9OH, C_3H_7OH, PEG, and glycerol) exhibited varying degrees of antimicrobial activity against the tested microorganisms. For instance, ZnO-2 (synthesized with C_2H_5OH) and ZnO-6 (synthesized with glycerol) generally demonstrated higher antimicrobial activity against Gram-positive bacteria, while ZnO-3 (synthesized with C_4H_9OH) showed superior efficacy against certain Gram-negative strains. These findings suggest that the physicochemical properties of ZnO-NPs, such as particle size, morphology, surface charge, and

crystallinity, are strongly influenced by the synthesis route, which in turn affects their interactions with microbial cells and their ability to generate ROS. Therefore, optimizing the synthesis parameters is crucial for enhancing the antimicrobial efficacy of ZnO-NPs and tailoring them for specific biomedical or environmental applications. Figures 7 and 8 provide comprehensive graphical comparisons of the antimicrobial activity of all six ZnO-NP formulations against Gram-positive and Gram-negative bacteria, respectively, alongside standard antibiotics. These visual representations highlight several key patterns. For Gram-positive bacteria (Figures 7 and 8), ZnO-2 and ZnO-6 generally demonstrated the highest activity, with ZnO-2 being particularly effective against *M. luteus* and ZnO-6 showing exceptional activity against *S. epidermidis* and *L. monocytogenes*. For Gram-negative bacteria (Figure 7, 9), ZnO-3 exhibited the highest overall activity, particularly against *K. pneumoniae*, while ZnO-1 and ZnO-2 showed notable efficacy against *E. coli* and *P. aeruginosa*, respectively. The differential activity of ZnO formulations against various pathogens suggests formulation-specific efficacy, which may be attributed to differences in physicochemical properties such as particle size, shape, surface charge, and crystallinity. The observed antimicrobial activity of ZnO-NPs can be attributed to multiple mechanisms. ZnO-NPs can produce hydrogen peroxide, hydroxyl radicals, and superoxide anions that cause oxidative stress and subsequent cell death (Figure 10). The varying efficacy of different ZnO formulations may be related to their differential ability to generate ROS. ZnO-NPs can interact directly with membrane components, leading to increased permeability and eventual cell lysis. The differential activity against Gram-positive and Gram-negative bacteria may be attributed to the structural differences in their cell walls. ZnO-NPs may bind to essential enzymes or disrupt electron transport chains, inhibiting vital cellular functions. Smaller NPs may penetrate bacterial cell walls more efficiently, leading to intracellular damage. The size, shape, and surface properties of the NPs play crucial roles in determining their antimicrobial efficacy. The observed variations in activity among the six ZnO formulations suggest differences in these physicochemical properties, which are largely determined by the synthesis method. Our findings regarding the superior activity of flower-like ZnO-6 align with those of Babayevska et al. [8] and Singh et al. [13], which reported that hierarchical nanostructures exhibit enhanced cytotoxicity due to increased surface roughness and area. Furthermore, the higher sensitivity of Gram-positive bacteria compared to Gram-negative strains observed in this study is consistent with previous reports [2, 3], attributing this difference to the protective outer membrane of Gram-negative bacteria. This comprehensive evaluation demonstrates that

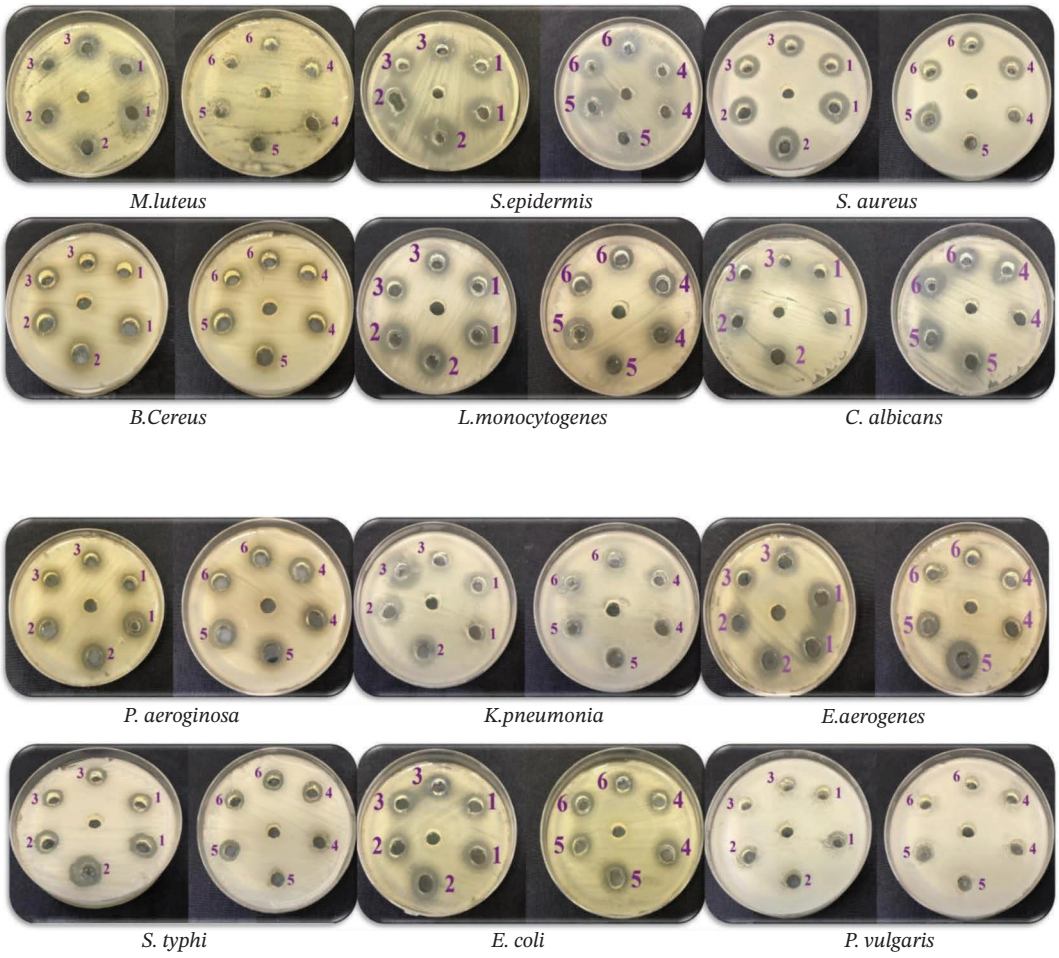

[1][ZnO-1-H_2O] [2][ZnO-2-C_2H_5OH] 3[ZnO-3-C_4H_9OH] [4][ZnO-4-C_3H_7OH] [5][ZnO-5-PEG] [6][ZnO-6-Glycerol]

FIGURE 7 | Antimicrobial activity (inhibition zone [mm]) of ZnO-NPs in Gram (−) and Gram (+) bacteria and yeast.

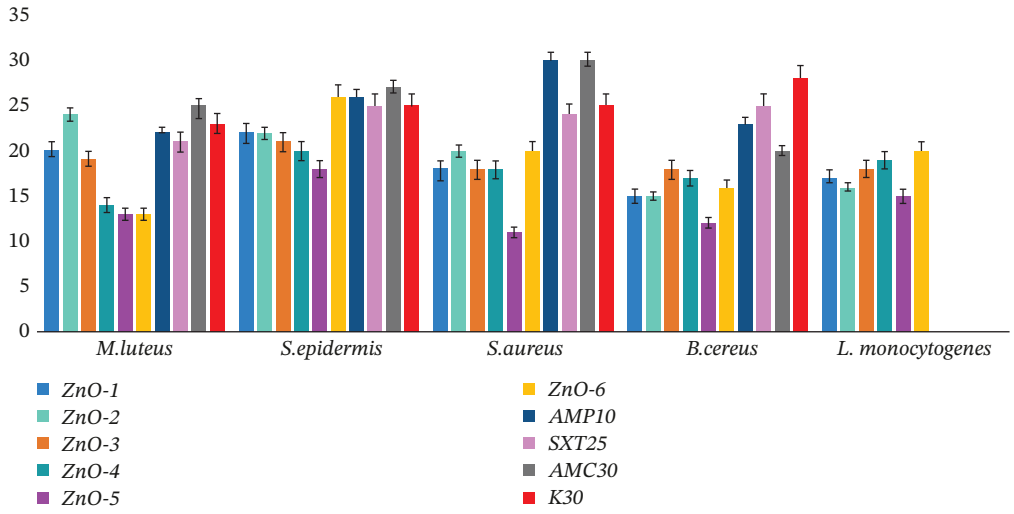

FIGURE 8 | Graphical illustration of Gram (+) pathogenic bacteria (*M.luteus, S.epidermis, S. aureus, B.cereus,* and *L.monocytogenes*) and standard reagents.

ZnO-NPs possess significant broad-spectrum antimicrobial activity against clinically relevant pathogens. The formulations ZnO-2, ZnO-3, and ZnO-6 showed particularly promising results, exhibiting comparable or superior activity to conventional antibiotics against several pathogens. The effectiveness of these NPs against both antibiotic-susceptible and resistant strains, such as *P. aeruginosa*, highlights their potential application in addressing the growing challenge of antimicrobial resistance. Furthermore, their dual antibacterial and antifungal properties make them attractive candidates for developing novel antimicrobial therapies for polymicrobial infections. Future research should focus on elucidating the precise mechanisms of action of these NPs, investigating their potential synergistic effects with conventional antibiotics, evaluating their safety and efficacy in in vivo models, developing targeted delivery systems to enhance their therapeutic potential while minimizing potential toxicity concerns, and optimizing synthesis methods to enhance specific antimicrobial properties against target pathogens. These findings provide a strong foundation for the development of ZnO-NP-based antimicrobial agents with potential applications in healthcare, food safety, and environmental protection.

3.3 | Cytotoxicity Assay Results

H460 cells were subjected to treatment with six different ZnO-NP formulations at concentrations ranging from 12.5 to 200 μg/mL over a 48-h exposure period. ZnO-1 demonstrated statistically significant cytotoxicity against H460 cells, with an IC50 of 48.6 μg/mL. ZnO-2 exhibited considerable cytotoxicity against H460 cells, with an IC_{50} of 38.1 μg/mL. ZnO-3 demonstrated potent cytotoxicity against H460 cells, with an IC_{50} of 42.3 μg/mL. ZnO-4 exhibited moderate cytotoxicity with an IC_{50} of 54.7 μg/mL. ZnO-5 demonstrated the lowest cytotoxicity among all formulations, with an IC50 of 67.8 μg/mL, indicating the highest biocompatibility profile among the tested NPs. ZnO-6 demonstrated particularly notable cytotoxicity against H460 cells, exhibiting the highest potency among all tested formulations, with an IC_{50} of 31.9 μg/mL, indicating superior anticancer potential that correlates with its highest surface area and unique floral morphology.

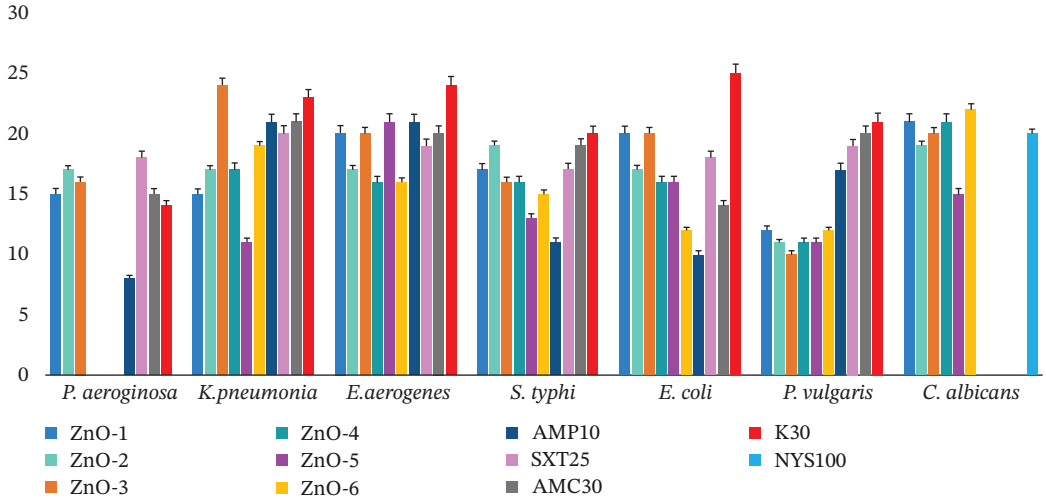

FIGURE 9 | Graphical illustration of Gram (−) pathogenic bacteria (*P. aeroginosa, K.pneumoniae, E.aerogenes, S. typhi, E. coli, P. vulgaris, and* C. albicans) and standard reagents.

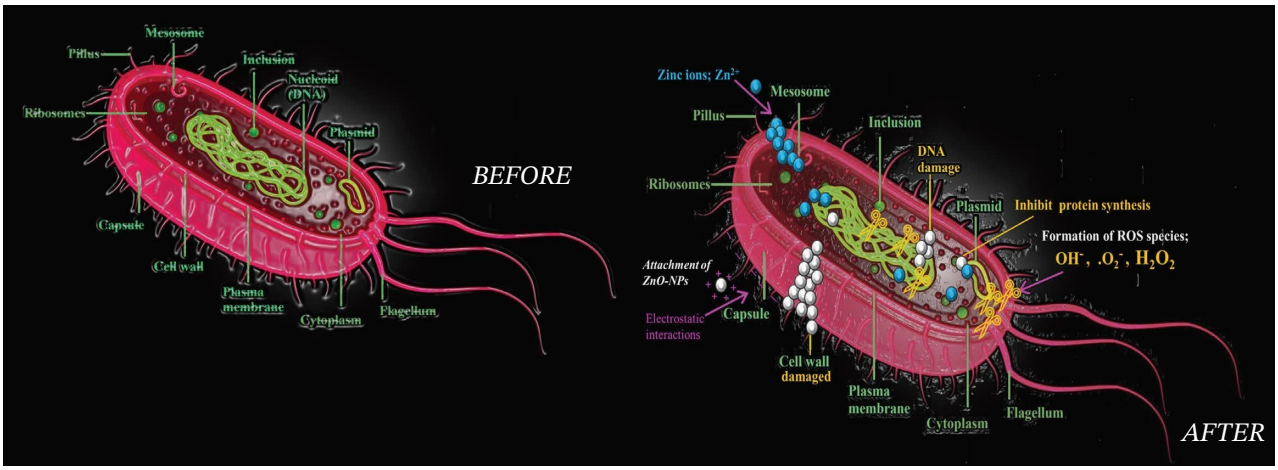

FIGURE 10 | Cell model for the main mechanism of bactericidal action of ZnO-NPs.

The cytotoxicity results revealed a clear correlation between the physicochemical properties of ZnO-NPs and their anticancer efficacy against H460 lung cancer cells. ZnO-6 exhibited the lowest IC_{50} value of 31.9 μg/mL, which directly correlates with its highest BET surface area of 1641.7 m^2/g among all tested formulations. This finding supports the established principle that an increased surface area enhances NP–cell interactions, leading to more efficient cellular uptake and subsequent cytotoxic effects. The superior performance of ZnO-6 can be attributed to its unique floral morphology, which provides multiple contact points with cancer cells and facilitates enhanced penetration through cellular membranes. ZnO-2 demonstrated the second-highest cytotoxicity, with an IC50 of 38.1 μg/mL, likely due to ethanol-mediated synthesis that imparted favorable particle characteristics for cellular interaction. ZnO-3 exhibited moderate cytotoxicity (IC50 = 42.3 μg/mL), suggesting that butanol synthesis affects particle properties. ZnO-1, synthesized with water showed an IC_{50} value of 48.6 μg/mL, representing baseline cytotoxic activity without organic solvent modification. ZnO-4 displayed reduced cytotoxicity with an IC_{50} value of 54.7 μg/mL, possibly due to its distinctive clover leaf morphology, which affects the cellular uptake efficiency. In contrast, ZnO-5 showed the highest IC50 value of 67.8 μg/mL, consistent with the biocompatibility-enhancing properties of PEG stabilization. The PEG coating creates a hydrophilic shell around the NPs, reducing their reactivity and cellular toxicity while improving biocompatibility. The glycerol-mediated synthesis of ZnO-6 appears to generate more reactive surface sites than other synthesis methods, thereby contributing to its enhanced cytotoxic potential. Furthermore, a notable correlation was observed between antimicrobial activity and cytotoxicity, with formulations exhibiting strong antibacterial activity, particularly ZnO-2 and

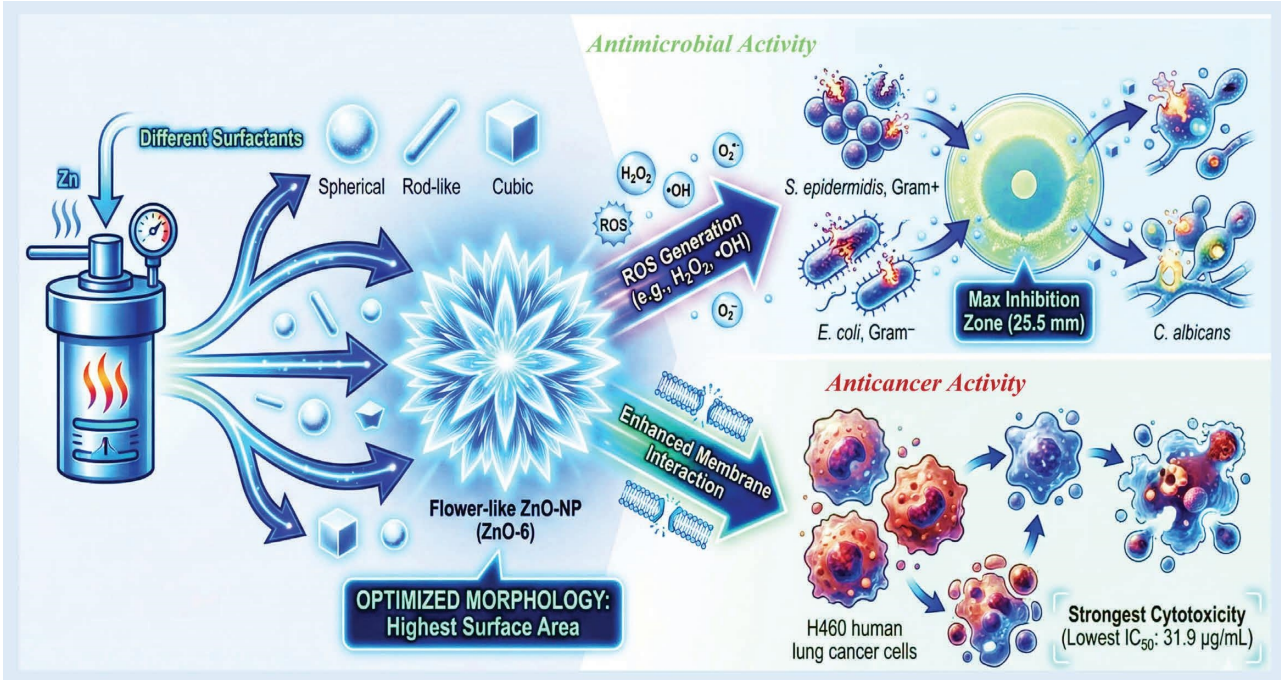

FIGURE 11 | Shape-directed hydrothermal design of ZnO-NPs for both antimicrobial and anticancer applications.

ZnO-6, also demonstrating lower IC_{50} values against cancer cells. This relationship suggests that the mechanisms underlying antimicrobial and anticancer activities may share common pathways, possibly involving the generation of ROS and membrane disruption. These findings are consistent with previous literature reports on ZnO-NPs against various cancer cell lines, confirming that morphology-dependent properties significantly influence therapeutic efficacy.

4 | Conclusions

In this study, the antimicrobial and anticancer properties of six different ZnO-NP formulations, synthesized using various solvents and surfactants, were evaluated in detail through hydrothermal synthesis (as shown in Figure 11). Spectroscopic and crystallographic analyses confirmed the successful synthesis of ZnO nanostructures. At the same time, microscopic examinations revealed that changes in synthesis conditions had significant effects on the morphological structures and dimensions of the NPs. The findings showed that ZnO-NPs exhibited a strong inhibitory effect, especially against Gram-positive bacteria. Furthermore, the ZnO-2, ZnO-3, and ZnO-6 formulations demonstrated superior antimicrobial activity against certain pathogenic strains compared to standard antibiotics. These results suggest that these NPs have potential as effective antimicrobial agents against pathogenic microorganisms or as additives to the existing antimicrobial products.

In addition, it has been shown that the physicochemical properties of NPs are greatly affected by the synthesis methods used and that these properties are directly determinants of antimicrobial activity. The fact that ZnO-NPs exhibit both antibacterial and antifungal properties indicates that these structures can be evaluated as alternative therapeutic agents against resistant microorganisms. In the future, the mechanisms of action of these NPs should be investigated in more detail, and their potential for clinical applications should be supported by in vivo biocompatibility analyses.

Author Contributions

E. H. Ö. and N. K. Y. designed and carried out the experiments, depending on the synthesis, and contributed to the interpretation of the results. N. K. Y. performed visualization, formal analysis, and writing–original draft. E. H. Ö. performed visualization, formal analysis, writing, original draft, review, and editing. H. Ö. carried out antimicrobial experiments and assessments. H. E. K. conducted cytotoxicity experiments and assessments. Each author contributed to the final manuscript and discussed the findings.

Acknowledgments

We would like to present our special thanks to Dr. M. KOC for his precious support. Kırklareli University Advanced Technologies Application and Research Center (ITUAM) is acknowledged for providing facilities. The 11th figure in this article was created with the help of Gemini AI. We acknowledge Gemini AI.

Funding

The authors declare that they received no funding for this research.

Conflicts of Interest

The authors declare no conflicts of interest.

Data Availability Statement

The data that support the findings of this study are included in the article, and further inquiries can be directed to the corresponding author.

References

1. S. Prashanna Suvaitha, "Novel Trimetallic Oxide (Cdo/Zno/V_2O_5) Nanocomposite Derived From Eggshell Membrane: Synthesis, Structural Characterization, Antibacterial and Antifungal Activities," *Surfaces and Interfaces* 56 (2025): 105677, https://doi.org/10.1016/j.surfin.2024.105677.

2. S. V. Gudkov, D. E. Burmistrov, D. A. Serov, M. B. Rebezov, A. A. Semenova, and A. B. Lisitsyn, "A Mini Review of Antibacterial Properties of ZnO Nanoparticles," *Frontiers in Physics* 9 (2021): 641481, https://doi.org/10.3389/fphy.2021.641481.

3. K. Gold, B. Slay, M. Knackstedt, and A. Gaharwar, "Antibacterial Activity of Metal and Metal-Oxide Based Nanoparticles," *Advanced Therapeutics* 1, no. 3 (2018): 1700033, https://doi.org/10.1002/adtp.201700033.11.

4. Y. Habboush and N. Guzman, "Antibiotic Resistance," *Stat Pearls* (2020): https://www.ncbi.nlm.nih.gov/books/NBK513277/.

5. World Health Organization, *World Health Statistics* (WHO, 2014), https://www.who.int/news/item/15-05-2014-world-health-statistics-2014.

6. B. Langford, M. So, S. Raybardhan, et al., "Bacterial Co-Infection and Secondary Infection in Patients With COVID-19: A Living Rapid Review and Meta-Analysis," *Clinical Microbiology and Infection* 26, no. 12 (2020): 1622–1629, https://doi.org/10.1016/j.cmi.2020.07.016.

7. E. Sharifipour, S. Shams, M. Esmkhani, et al., "Evaluation of Bacterial Co-Infections of the Respiratory Tract in COVID-19 Patients Admitted to ICU," *BMC Infectious Diseases* 20, no. 1 (2020): 646, https://doi.org/10.1186/s12879-020-05374-z.

8. N. Babayevska, Ł. Przysiecka, I. Iatsunskyi, et al., "ZnO Size and Shape Effect on Antibacterial Activity and Cytotoxicity Profile," *Scientific Reports* 12, no. 1 (2022): 8148, https://doi.org/10.1038/s41598-022-12134-3.

9. A. Woźniak, A. Malankowska, G. Nowaczyk, et al., "Size and Shape-Dependent Cytotoxicity Profile of Gold Nanoparticles for Biomedical Applications," *Journal of Materials Science: Materials in Medicine* 28, no. 6 (2017): 92, https://doi.org/10.1007/s10856-017-5902-y.

10. Q. Li, L. Ye, A. Zhang, and Z. Feng, "The Preparation and Morphology Control of Heparin-Based pH Sensitive Polyion Complexes and Their Application as Drug Carriers," *Carbohydrate Polymers* 211 (2019): 370–379, https://doi.org/10.1016/j.carbpol.2019.01.089.

11. L. Zhang, F. Gu, J. Chan, A. Wang, R. Langer, and O. Farokhzad, "Nanoparticles in Medicine: Therapeutic Applications and Developments," *Clinical Pharmacology and Therapeutics* 83, no. 5 (2008): 761–769, https://doi.org/10.1038/sj.clpt.6100400.

12. W. Wenting, et al., "Antibacterial Behaviors of Cu_2O Particles With Controllable Morphologies in Acrylic Coatings," *Applied Surface Science* 465 (2019): 279–287, https://doi.org/10.1016/j.apsusc.2018.09.184.

13. R. Singh, K. Verma, A. Patyal, I. Sharma, P. Barman, and D. Sharma, "Nanosheet and Nanosphere Morphology Dominated Photocatalytic and Antibacterial Properties of ZnO Nanostructures," *Solid State Sciences* 89 (2019): 1–14, https://doi.org/10.1016/j.solidstatesciences.2018.12.011.

14. P. Asanithi, S. Chaiyakun, and P. Limsuwan, "Growth of Silver Nanoparticles by DC Magnetron Sputtering," *Journal of Nanomaterials* 1 (2012): 963609, https://doi.org/10.1155/2012/963609.

15. H. Wender, P. Migowski, A. F. Feil, S. R. Teixeira, and J. Dupont, "Sputtering Deposition of Nanoparticles onto Liquid Substrates: Recent Advances and Future Trends," *Coordination Chemistry Reviews* 257, no. 17-18 (2013): 2468–2483, https://doi.org/10.1016/j.ccr.2013.01.013.

16. C. Binns, P. Prieto, S. Baker, et al., "Preparation of Hydrosol Suspensions of Elemental and Core–Shell Nanoparticles by co-Deposition

With Water Vapour from the Gas-Phase in Ultra-High Vacuum Conditions," *Journal of Nanoparticle Research* 14, no. 9 (2012): 1–16, https://doi.org/10.1007/s11051-012-1136-6.

17. E. Hasanoğlu Özkan, N. Aslan, M. M. Koç, et al., "Fe_3O_4 Nanoparticle Decorated Novel Magnetic Metal Oxide Microcomposites for the Catalytic Degradation of 4-Nitrophenol for Wastewater Cleaning Applications," *Journal of Materials Science: Materials in Electronics* 33 (2022): 1039–1053, https://doi.org/10.1007/s10854-021-07376-2.

18. C. D. De Souza, B. R. Nogueira, and M. E. C. Rostelato, "Review of the Methodologies Used in the Synthesis Gold Nanoparticles by Chemical Reduction," *Journal of Alloys and Compounds* 798 (2019): 714–740, https://doi.org/10.1016/j.jallcom.2019.05.153.

19. T. Shao, Q. Yin, J. Bai, J. Zhu, and M. Gan, "Adsorption and Catalytic Reduction of Hexavalent Chromium Based on Nanomaterials: A Review on Metal, Metallic Oxide, Metallic Sulfide and Carbon-Based Catalyst," *Environmental Research* 266 (2025): 120449, https://doi.org/10.1016/j.envres.2024.120449.

20. S. Soni, A. Kumari, S. Kumari, et al., "Base Metals (Ni, Cu, Zn, Fe) Oxide Nanomaterials Mediated Photo/Sono-Catalytic Removal of Emerging Pharmaceutical Contaminants From Wastewater," *Journal of Environmental Chemical Engineering* 12, no. 6 (2024): 114683, https://doi.org/10.1016/j.jece.2024.114683.

21. N. Aslan, B. Ceylan, M. M. Koç, and F. Findik, "Metallic Nanoparticles as X-Ray Computed Tomography (CT) Contrast Agents: A Review," *Journal of Molecular Structure* 1219, no. 1 (2020): 128599, https://doi.org/10.1016/j.molstruc.2020.128599.

22. M. M. Koç, N. Aslan, A. P. Kao, and A. H. Barber, "Evaluation of X-Ray Tomography Contrast Agents: A Review of Production, Protocols, and Biological Applications," *Microscopy Research and Technique* 82, no. 6 (2019): 812–848, https://doi.org/10.1002/jemt.23225.

23. M. M. Koç, U. Paksu, N. Kurnaz Yetim, B. Coşkun, E. Hasanoğlu Özkan, and M. Erkovan, "Nanoparticles in Photothermal Therapy-Based Medical and Theranostic Applications: An Extensive Review," *The European Physical Journal Plus* 140 (2025): 514, https://doi.org/10.1140/epjp/s13360-025-06452-4.

24. G. S. Keleşoğlu, M. Özdinçer, A. Dalmaz, K. Zenkin, and S. Durmuş, "Green Synthesis and Structural Characterization of ZnO Nanoparticles and ZnO@TiO_2 Nanocomposites by Cinnamomum Verum Bark Extract," *Turkish Journal of Analytical Chemistry* 5, no. 2 (2023): 118–123, https://doi.org/10.51435/turkjac.1395817.

25. V. N. Kalpana and V. Devi Rajeswari, "A Review on Green Synthesis, Biomedical Applications, and Toxicity Studies of ZnO NPs," *Bioinorganic Chemistry and Applications* 2018, no. 1 (2018): 1–12, https://doi.org/10.1155/2018/3569758.

26. P. K. Mishra, H. Mishra, A. Ekielski, S. Talegaonkar, and B. Vaidya, "Zinc Oxide Nanoparticles: A Promising Nanomaterial for Biomedical Applications," *Drug Discovery Today* 22, no. 12 (2017): 1825–1834, https://doi.org/10.1016/j.drudis.2017.08.006.

27. C. Hanley, J. Layne, A. Punnoose, et al., "Preferential Killing of Cancer Cells and Activated Human T Cells Using ZnO Nanoparticles," *Nanotechnology* 19, no. 29 (2008): 295103, https://doi.org/10.1088/0957-4484/19/29/295103.

28. R. Anitha, K. V. Ramesh, T. N. Ravishankar, K. H. Sudheer Kumar, and T. Ramakrishnappa, "Cytotoxicity, Antibacterial and Antifungal Activities of ZnO Nanoparticles Prepared by the Artocarpus gomezianus Fruit Mediated Facile Green Combustion Method," *Journal of Science: Advanced Materials and Devices* 3, no. 4 (2018): 440e451–451, https://doi.org/10.1016/j.jsamd.2018.11.001.

29. M. Ahmad, E. Ahmed, F. Zafar, et al., "Enhanced Photocatalytic Activity of Ce Doped ZnO Nanopowders Synthesized by Combustion Method," *Journal of Rare Earths* 33, no. 3 (2015): 255e262–262, https://doi.org/10.1016/S1002-0721(14)60412-9.

30. V. Krishnamoorthy, D. B. Hiller, R. Ripper, et al., "Epinephrine Induces Rapid Deterioration in Pulmonary Oxygen Exchange in Intact, Anesthetized Rats: A Flow and Pulmonary Capillary Pressure-Dependent Phenomenon," *Anesthesiology* 117, no. 4 (2012): 745–754, https://doi.org/10.1097/ALN.0b013e31826a7da7.

31. N. Kurnaz Yetim, "Hydrothermal Synthesis of Co_3O_4 With Different Morphology: Investigation of Magnetic and Electrochemical Properties," *Journal of Molecular Structure* 1226 (2020): 129414, https://doi.org/10.1016/j.molstruc.2020.129414.

32. N. Kurnaz Yetim, E. Hasanoğlu Özkan, and H. Öğütçü, "Use of Co_3O_4 Nanoparticles With Different Surface Morphologies for Removal of Toxic Substances and Investigation of Antimicrobial Activities via *In Vivo* Studies," *Environmental Science and Pollution Research* 30, no. 48 (2023): 106585–106597, https://doi.org/10.1007/s11356-023-29879-7.

33. C. Tuncer, "Hydrothermal Synthesis and Sol-Gel Methods for CdS Particle Production in Different Morphologies and Their Use in Wastewater Applications," *Sakarya University Journal of Science* 22, no. 3 (2018): 888–897, https://dergipark.org.tr/en/pub/saufenbilder/issue/30828/321585.

34. N. Kati and B. Ayten, "Investigation of Structural and Optical Properties of Boron-Doped ZnO Nanomaterials Synthesized by Hydrothermal Method," *Journal of the Indian Chemical Society* 102, no. 6 (2025): 101706, https://doi.org/10.1016/j.jics.2025.101706.

35. L. Zhang, H. Zhang, and B. Jiang, "ZnO Nanostructures Fabricated by a Two-Step Hydrothermal Method for Enhanced Ethanol Sensing," *Microchemical Journal* 209 (2025): 112896, https://doi.org/10.1016/j.microc.2025.112896.

36. M. Ebrahimifar, I. Kazeminezhad, and A. Rahimi, "In Situ Hydrothermal Synthesis of $ZnCo_2O_4$/ZnO Nanocomposite: Structural, Optical, Electrochemical Properties and Photocatalytic Performance Under Visible Light," *Optik* 312 (2024): 171976, https://doi.org/10.1016/j.ijleo.2024.171976.

37. Md. Elias, R. Alam, S. Khatun, et al., "Hydrothermal Synthesis of Carboxylated Functionalized Jute Stick Carbon and Reduced Graphene Oxide Based ZnO Nanocomposite Photocatalysts: A Comparative Study," *Journal of Industrial and Engineering Chemistry* 143 (2025): 424–436, https://doi.org/10.1016/j.jiec.2024.08.049.

38. S. Alaguvel, S. K. Kalifathullah, and S. Devikala, "Unraveling the Synergistic Effects of ZnO and Ag@Zno Nanoparticles: an *In Vitro* Investigation of Anti-Cancer, Anti-Inflammatory, Antioxidant, and Antibacterial Properties," *Inorganic Chemistry Communications* 178, no. 1 (2025): 114522, https://doi.org/10.1016/j.inoche.2025.114522.

39. E. Alp, F. Olivieri, M. Aulitto, et al., "The Effect of ZnO Nanoparticles Morphology on the Barrier and Antibacterial Properties of Hybrid ZnO/Graphene Oxide/Montmorillonite Coatings for Flexible Packaging," *Surfaces and Interfaces* 55 (2024): 105307, https://doi.org/10.1016/j.surfin.2024.105307.

40. F. Yang, Y. Li, J. Xu, Y. Kang, B. Mu, and A. Wang, "Reconciling the Monodispersity of Bioinspired ZnO Nanoparticles on Palygorskite Nanorods for a Well-Balanced Antibacterial Effect and Biocompatibility," *Ceramics International* 50, no. 19 (2024): 35236–35246, https://doi.org/10.1016/j.ceramint.2024.06.332.

41. E. Hasanoğlu Özkan, "Detection of 4-Nitrophenol in Wastewater Using Microstructures of Various Morphologies," *Journal of Molecular Structure* 1274, no. 2 (2023): 134564, https://doi.org/10.1016/j.molstruc.2022.134564.

42. S. Çalışkan, E. Hasanoğlu Özkan, N. Kurnaz Yetim, et al., "Aluminum (III) Ions Removal From Drinking Water Samples by Flower Like ZnO Nanoparticles With Solid Phase Extraction," *Water, Air, and Soil Pollution: International Journal of Environment and Pollution* 236 (2025): 224, https://doi.org/10.1007/s11270-025-07886-3.

43. S. Korkmaz, E. Hasanoğlu Ozkan, D. Uzun, N. Kurnaz Yetim, and C. Özcan, "Magnetic Solid Phase Extraction of Lead (II) and Cadmium

(II) From Water Samples Using ZnO@Fe_3O_4 Nanoparticles Combined With Flame Atomic Absorption Spectrometry Determination," *Journal of Separation Science* 48, no. 3 (2025): e70115, https://doi.org/10.1002/jssc.70115.

44. E. A. Berberoğlu, M. M. Koç, N. Kurnaz Yetim, and C. Özcan, "Highly Efficient ZnO Nanoflowers for the Removal of Highly Toxic Aqueous Pb(II) and Cr(VI)," *Journal of the Iranian Chemical Society* 20, no. 11 (2023): 2821–2830, https://doi.org/10.1007/s13738-023-02878-8.

45. D. Nartop, E. Hasanoglu Ozkan, M. Gündem, et al., "Synthesis, Antimicrobial and Antimutagenic Effects of Novel Polymeric-Schiff Bases Including Indol," *Journal of Molecular Structure* 1195 (2019): 877–882, https://doi.org/10.1016/j.molstruc.2019.06.042.

46. D. Nartop, B. Demirel, M. Güleç, et al., "Novel Polymeric Microspheres: Synthesis, Enzyme Immobilization, Antimutagenic Activity, and Antimicrobial Evaluation Against Pathogenic Microorganisms," *Journal of Biochemical and Molecular Toxicology* 34, no. 2 (2020): e22432, https://doi.org/10.1002/jbt.22432.

47. M. Anar, E. Hasanoğlu Özkan, H. Ogutcu, G. Ağar, I. Şakıyan, and N. Sarı, "Useful Agents Against Aflatoxin B_1-Antibacterial Azomethine and Mn(III) Complexes Involving L-Threonine, L-Serine, and L-Tyrosine," *Artificial Cells, Nanomedicine, and Biotechnology* 44, no. 3 (2016): 853–858, https://doi.org/10.3109/21691401.2014.991792.

48. D. Nartop, E. Tokmak, E. Hasanoglu Ozkan, et al., "Synthesis of Novel Polymers Containing Schiff Base as Potential Antimutagenic and Antimicrobial Agents," *Journal of Medicinal and Chemical Sciences* 4, no. 3 (2020): 363–372, https://doi.org/10.26655/jmchemsci.2020.4.6.

49. C. L. B. Graham, H. Newman, F. N. Gillett, et al., "A Dynamic Network of Proteins Facilitate Cell Envelope Biogenesis in Gram-Negative Bacteria," *International Journal of Molecular Sciences* 22, no. 23 (2021): 12831, https://doi.org/10.3390/ijms222312831.

50. E. Ülke, E. Hasanoğlu Özkan, D. Nartop, and H. Öğütcü, "New Antimicrobial Polymeric Microspheres Containing Azomethine," *Journal of Inorganic and Organometallic Polymers and Materials* 32 (2022): 3971–3982, https://doi.org/10.1007/s10904-022-02411-z.

51. T. L. Riss and R. A. Moravec, "Use of Multiple Assay Endpoints to Investigate the Effects of Incubation Time, Dose of Toxin, and Plating Density in Cell-Based Cytotoxicity Assays," *Assay and Drug Development Technologies* 2, no. 1 (2004): 51–62, https://doi.org/10.1089/154065804322966315.

52. M. Yildirim, E. Aksakal, F. B. Ozgeris, B. Ozgeris, and A. Gorme, "Biological Evaluation of Azide Derivative as Antibacterial and Anticancer Agents," *Natural Products and Biotechnology* 2, no. 2 (2022): 105–113, https://doi.org/10.58465/natprobiotech.2022.11.

53. M. A. Ismail, K. K. Taha, A. Modwi, and L. Khezami, "ZnO Nanopartıcles: Surface and X-Ray Profile Analysis," *Journal of Ovonic Research* 14, no. 5 (2018): 381–393.

54. A. K. Arora, S. Devi, V. S. Jaswal, J. Singh, M. Kinger, and V. D. Gupta, "Synthesis and Characterization of ZnO Nanoparticles," *Oriental Journal of Chemistry* 30, no. 4 (2014): 1671–1679.

55. N. M. Shamhari, B. S. Wee, S. F. Chin, and K. Y. Kok, "Synthesis and Characterization of Zinc Oxide Nanoparticles With Small Particle Size Distribution," *Acta Chimica Slovenica* 65, no. 3 (2018): 578–585, https://doi.org/10.17344/acsi.2018.4213.

56. S. W. Bian, I. A. Mudunkotuwa, T. Rupasinghe, and V. H. Grassian, "Aggregation and Dissolution of 4 Nm ZnO Nanoparticles in Aqueous Environments: Influence of pH, Ionic Strength, Size, and Adsorption of Humic Acid," *Langmuir* 27, no. 10 (2011): 6059–6068, https://doi.org/10.1021/la200570n.